

Subpixel image reconstruction using nonuniform defocused images

Nguyen Hieu Thao, Oleg Soloviev,
Jacques Noom and Michel Verhaegen

the date of receipt and acceptance should be inserted later

Abstract This paper considers the problem of reconstructing an object with high-resolution using several low-resolution images, which are degraded due to *nonuniform defocus effects* caused by angular misalignment of the subpixel motions. The new algorithm, indicated by the Superresolution And Nonuniform Defocus Removal (SANDR) algorithm, simultaneously performs the nonuniform defocus removal as well as the superresolution reconstruction. The SANDR algorithm combines non-sequentially the nonuniform defocus removal method recently developed by Thao *et al.* and the least squares approach for subpixel image reconstruction. Hence, it inherits global convergence from its two component techniques and avoids the typical error amplification of multi-step optimization contributing to its robustness. Further, existing acceleration techniques for optimization have been proposed that assure fast convergence of the SANDR algorithm going from rate $\mathcal{O}(1/k)$ to $\mathcal{O}(1/k^2)$ compared to most existing superresolution (SR) techniques using the gradient descent method. An

This project has received funding from the ECSEL Joint Undertaking (JU) under grant agreement No. 826589. The JU receives support from the European Union's Horizon 2020 research and innovation programme and Netherlands, Belgium, Germany, France, Italy, Austria, Hungary, Romania, Sweden and Israel.

Nguyen Hieu Thao

Delft Center for Systems and Control, Delft University of Technology, 2628CD Delft, The Netherlands. Department of Mathematics, School of Education, Can Tho University, Can Tho, Vietnam. E-mail: h.t.nguyen-3@tudelft.nl, nhthao@ctu.edu.vn

Oleg Soloviev

Delft Center for Systems and Control, Delft University of Technology, 2628CD Delft, The Netherlands. Flexible Optical B.V., Polakweg 10-11, 2288 GG Rijswijk, The Netherlands. E-mail: o.a.soloviev@tudelft.nl

Jacques Noom

Delft Center for Systems and Control, Delft University of Technology, 2628CD Delft, The Netherlands. E-mail: j.noom@tudelft.nl

Michel Verhaegen

Delft Center for Systems and Control, Delft University of Technology, 2628CD Delft, The Netherlands. E-mail: m.verhaegen@tudelft.nl

extensive simulation study evaluating the new SANDR algorithm has been conducted. As no algorithms are available to address the combined problem, in this simulation study we restrict the comparison of SANDR with other SR algorithms neglecting the defocus aberrations. Even for this case the advantages of the SANDR algorithm have been demonstrated.

Keywords Superresolution, Image reconstruction, Computational imaging, Deconvolution, Inverse problems

1 Introduction

Image-based quality control is one of the important tools used during the manufacturing and end quality checks in semiconductor [9], automotive [32], and many other industries. For Industry 4.0, requiring a fully automatized quality checks, the spatial resolution (size of the smallest feature that can be inspected) is the key factor that affects the overall efficiency and throughput of the control tool. For high-quality imaging systems used in these tools, the spatial resolution is defined as the quotient between the pixel size and the magnification, and thus for a higher resolution, either a smaller pixel size or a larger magnification is required. Larger magnification corresponds to smaller field of view (FOV in Fig. 1), often it is desirable to have a smaller pixel size. However, there are technological and design limits to the magnification and the smallest pixels that can be manufactured and/or used in these tools and thus a computational approach to increasing spatial resolution provides an interesting alternative. The reconstruction of an object with high-resolution from several low-resolution (LR) images capturing the object at subpixel-offset positions, called the *SuperResolution* (SR) problem, has been studied for many decades [19, 26]. A number of solution approaches have been proposed for the SR problem, including direct methods [12, 13] and iterative algorithms [4, 7, 8, 14, 16, 18, 21, 22, 28, 30, 31].

Superresolution reconstruction is possible if the LR images are registered for different subpixel-offset positions of the object. In practice, shifting the object at subpixel scale can be a major challenge to the SR problem and gives rise to a number of important questions that need to be addressed. Camera shake and motion blur induced by the shifts have been analyzed in [1, 11]. Inaccuracy of subpixel registration has been considered in [15, 24]. Ideally, the shifting process should not cause any variations in the object orientation with respect to the camera. However, this is not always the case in practice and such deviations cause undesirable deterioration of the data images and thus the reconstruction. Imprecise displacements with respect to the optical axis would introduce defocus blurs in the acquired images. More challenging, the shifting process can induce rotational movements of the object causing *nonuniform defocus effects* in the data. To the best of our knowledge, the latter challenge has not been considered in the literature of SR by subpixel motions.

In this paper, we consider the problem of reconstructing a Superresolution Image using Nonuniform Defocused images, called the SIND problem. Our

consideration was primarily motivated by the inspection of wafers in semiconductor industry and the basic hypotheses are mainly inspired by its practical context, but the resulting solution is also scalable for similar applications of computer vision. As an alternative to shifting the object, LR images can be registered using multiple cameras whose optical axes are typically at different directions towards the object. This also results in *nonuniform defocus blurs* in the acquired data, and the SIND problem covers this challenge as a special case with known and fixed blurs.

Solution approaches to the SIND problem should address three main tasks, including estimation of nonuniform defocus models, removal of nonuniform defocus effects, and reconstruction of an SR image. Assuming that the nonuniform defocus models have been estimated, this paper is devoted to the last two tasks. More specifically, we propose a new algorithm to simultaneously perform both Superresolution reconstruction And Nonuniform Defocus Removal (SANDR). The SANDR algorithm combines the nonuniform defocus removal method recently developed in [25] and the least squares approach [27] for subpixel image reconstruction but not in a sequential manner. Hence, it inherits global convergence from its two component techniques and avoids the typical error amplification of multi-step optimization contributing to its robustness. Further, existing acceleration techniques for optimization [2] have been proposed that assure fast convergence of the SANDR algorithm going from rate $\mathcal{O}(1/k)$ to $\mathcal{O}(1/k^2)$ compared to most existing SR techniques using the gradient descent method, where k is the number of iterations.

As, to our knowledge, no algorithms are available to address the SIND problem, we demonstrate the advantages of the SANDR algorithm over other SR algorithms neglecting the defocus aberrations, see Sect. 4.1. It is important to mention that the Projected Gradient (PG) and the so-called Sequential Minimization (SM) algorithms reported along with SANDR in the numerical section are also considered for the SIND problem for the first time. Hence, comparing the SANDR algorithm with them is not a goal of this paper.

2 Problem formulation

2.1 Superresolution by subpixel motions

Let o_m be the LR images, created by an imaging system, that sample image o of some planar object, see Fig. 1. Let each o_m be registered with some subpixel offset v_m , with coordinates expressed in pixels of o_m . We have the following sampling:

$$o_m \sim T_{v_m}(o), \quad (m = 1, 2, \dots, M), \quad (1)$$

where T_v denotes the translation by a vector v .

Let O be the SR image to be reconstructed. The ratio between the sizes of O and o_m is called the *superresolution factor* and denoted by τ . In this paper, the images are assumed to be square and the superresolution factor is the same in both row and column directions for the sake of brevity. As the

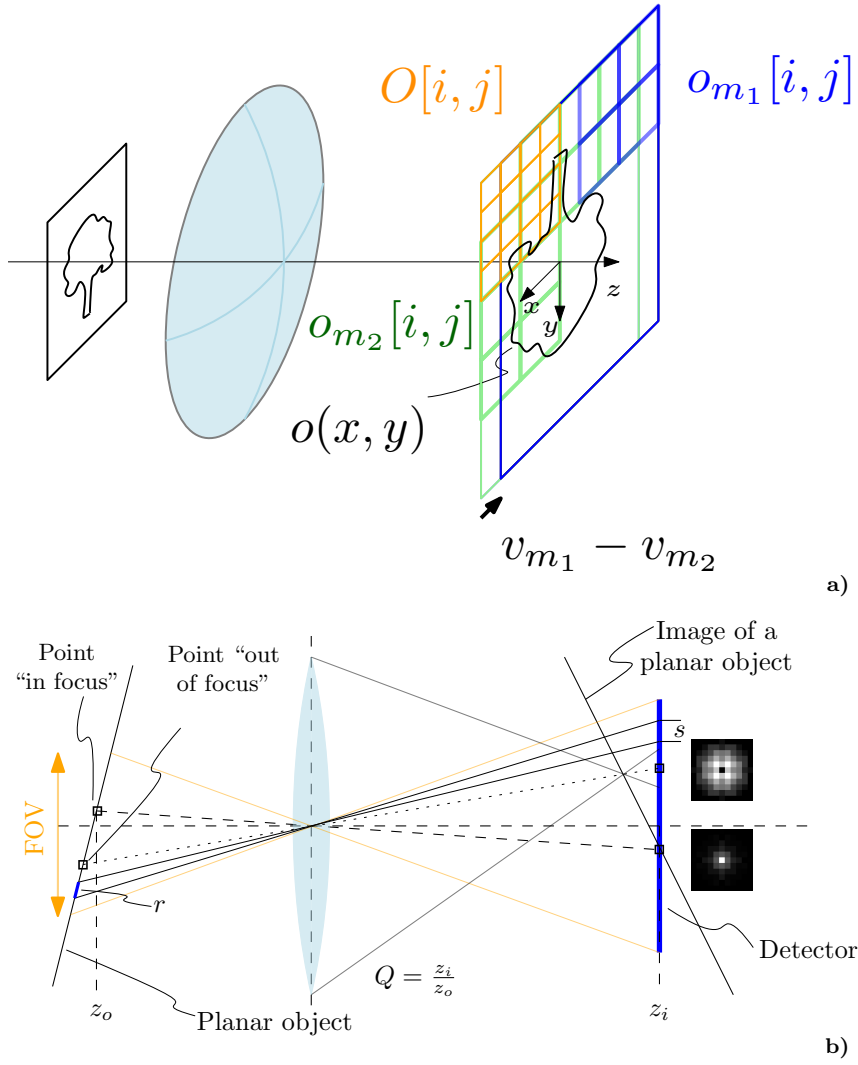


Fig. 1 a) Imaging scheme used in the problem formulation. An imaging lens with magnification Q creates image $o(x, y)$ of some planar object, which is registered by a detector with pixel size s to obtain M sampled images $o_m[i, j]$ (green, blue), with introduced subpixel offsets v_m in each of them. The superresolution problem is to restore $O[i, j]$ representing $o(x, y)$ sampled with a finer grid (orange). b) Side view of the imaging scheme with an example of misalignment of the object and detector planes creating position-dependent defocus blur.

shifts are measured in pixels of o_m , their coordinates with respect to O should be scaled up by τ . Then we also have the following sampling:

$$T_{\tau v_m}(O) \sim T_{v_m}(o), \quad (m = 1, 2, \dots, M). \quad (2)$$

The combination of (1) and (2) leads to the following superresolution model:

$$o_m \simeq D_\tau \circ T_{\tau v_m}(O), \quad (m = 1, 2, \dots, M), \quad (3)$$

where D_τ is the *downsampling operator* with rate τ , see Sect. 2.5 for the definition.

Remark 1 (external blurs) The imaging model (3) can be extended as follows [3, 5, 7, 8, 10, 14, 16, 17, 22, 23, 28, 30, 31]:

$$o_m \simeq D_\tau \circ H_m \circ T_{\tau v_m}(O), \quad (m = 1, 2, \dots, M),$$

where H_m denote the external blurs often modelled as isoplanatic convolutions and assumed to be known. For our target application in wafer inspection, external blurs are not so relevant and thus left for brevity though they do not add major challenge to the problem under consideration. Instead, we handle the more challenging anisoplanatic blurs induced by angular misalignment of the shifts as detailed in the next section.

2.2 Nonuniform defocus effects

In practice, the subpixel shifts can be accomplished by moving either the sample or the detector chip. In both cases, some angular misalignment can be introduced, which can be difficult or costly (*e.g.*, in terms of time/overall throughput) to eliminate completely. Figure 1b shows an example of a misaligned sample; a similar picture could be drawn for a misaligned detector, where geometrical distortions might also appear.¹ For simplicity, we do not discriminate between the object and detector misalignment. Depending on the particular realisation and on the optical magnification of the system, this might create presence of position-dependent defocus blur in the image, which, as we show later, prevents the direct application of existing superresolution algorithms.

We consider the challenge that the displacement process induces undesirable rotational movements of the object and the acquired images are degraded by nonuniform defocus blurs. In this case, the theoretical LR images o_m and the measured ones i_m are related by

$$i_m \simeq B_m(o_m), \quad (m = 1, 2, \dots, M), \quad (4)$$

where the blur operators B_m will be detailed shortly.

Let o_m situate in N defocus zones denoted by D_n ($n = 1, 2, \dots, N$), for each of which the Point Spread Function (PSF) is modelled using the Fourier transform [6]:

$$p_n = \left| \mathcal{F} \left(A \cdot e^{j d_n Z_2^0} \right) \right|^2 \quad (n = 1, 2, \dots, N), \quad (5)$$

¹ In this paper, we consider the geometrical distortions to be negligible compared to the position-dependent blur.

where the amplitude, product and square operations are elementwise, \mathcal{F} is the two-dimensional Fourier transform, A is the binary mask representing the camera aperture,² $j = \sqrt{-1}$ is the imaginary unit, d_n is the (directional) distance from D_n to the focal plane, and Z_2^0 is the Zernike polynomial of order two and azimuthal frequency zero.

We make use of the following model of nonuniform defocus blurs, whose physical relevance has been demonstrated, *e.g.*, in [25]:

$$B_m(o_m) = \sum_{n=1}^N (\mu_{mn} \cdot o_m) * p_n, \quad (m = 1, 2, \dots, M), \quad (6)$$

where $*$ is the two-dimensional convolution, μ_{mn} are the mask functions of o_m defined by: for $n = 1, 2, \dots, N$,

$$\mu_{mn}[i, j] = \begin{cases} 1 & \text{if } o_m[i, j] \in D_n, \\ 0 & \text{otherwise.} \end{cases}$$

This paper considers planar objects and d_n take the following form [25, Sect. IIC,]:

$$d_n = d(n_0 - n), \quad (n = 1, 2, \dots, N), \quad (7)$$

where d is the *Depth of Focus* (DoF) and n_0 is the *focal position*. The number of defocus zones N defines the degree of defocus in an image and can be different for each o_m . For brevity, it is taken the same in this paper.

The combination of (5), (6) and (7) yields the following blur model: ($m = 1, 2, \dots, M$)

$$B_m(o_m) = \sum_{n=1}^N (\mu_{mn} \cdot o_m) * \left| \mathcal{F} \left(A \cdot e^{jd(n_0-n)Z_2^0} \right) \right|^2. \quad (8)$$

2.3 The SIND problem

We consider the problem of reconstructing the Superresolution Image O from the Nonuniform Defocused images i_m according to the relations (3) and (4), where B_m are given by (8). It is referred to as the SIND problem.

2.4 Optimization formulations

Combining (3) and (4) yields the imaging model:

$$i_m = B_m \circ D_\tau \circ T_{\tau v_m}(O) + w_m, \quad (m = 1, 2, \dots, M), \quad (9)$$

where B_m are given by (8), and w_m represent the discrepancies between the theoretical and the measured data, *e.g.*, due to noise and model deviations.

² We assume that the diffraction-limited PSF is not resolved by the camera pixels.

In this paper, w_m are assumed to be independent zero-mean random variables with jointly Gaussian-distributed entries.³ For each $m = 1, 2, \dots, M$, let \mathcal{W}_m be the covariance matrix of $\mathbf{Vec}(w_m)$, where \mathbf{Vec} denotes the vectorization operator. Then the *maximum-likelihood* approach, *e.g.*, [27, Sect. 4.5.5.], applied to (9) leads to the following minimization problem:

$$\min_O f(O) + \mathcal{G}(O), \quad (10)$$

where \mathcal{G} is the regularization capturing the physical attributes of O (see Sect. 3.1), and f represents the data fidelity given by

$$f(O) = \sum_{m=1}^M R_m(O)^T \mathcal{W}_m^{-1} R_m(O), \quad (11)$$

where R_m ($m = 1, 2, \dots, M$) are the fitting residual errors for the (blurred) LR images:

$$R_m(O) = \mathbf{Vec}(B_m \circ D_\tau \circ T_{\tau v_m}(O) - i_m).$$

Remark 2 (sequential optimization) The residual error in (3) is mainly due to the inaccuracy of the subpixel shifts while the one in (4) is more related to measurement noise and model deviations of (8). When the latter is less severe than the former,⁴ one can also address (4) and (3) sequentially via the following two-step optimization:

$$\min_O \sum_{m=1}^M S_m(O)^T \Sigma_m^{-1} S_m(O) + \mathcal{G}(O), \quad (12)$$

where for $m = 1, 2, \dots, M$,

$$\begin{aligned} S_m(O) &= \mathbf{Vec}(D_\tau \circ T_{\tau v_m}(O) - \hat{o}_m), \\ \hat{o}_m &\in \arg \min_{o_m} Q_m(o_m)^T \mathcal{E}_m^{-1} Q_m(o_m) + \mathcal{H}(o_m), \\ Q_m(o_m) &= \mathbf{Vec}(B_m(o_m) - i_m). \end{aligned} \quad (13)$$

In the above, Σ_m and \mathcal{E}_m are respectively the covariance matrices representing the noise in (4) and (3), and \mathcal{H} is the regularization capturing the physical attributes of o_m . Sequentially minimizing (13) and (12) gives rise to the so-called SM algorithm (see Sect. 3.2), which suffers the typical error amplification of multi-step optimization compared to the proposed solution method for solving (10), see Sect. 4.3&4.4.

³ This assumption is ubiquitous and it does not rule out the case of Poisson noise as the latter can be well approximated by a Gaussian distribution in view of the central limit theorem provided that the image is registered with a sufficiently large number of photon counts.

⁴ This is relevant to wafer inspection, where the camera is high-quality while inexactness of the subpixel shifts poses the major challenge.

2.5 Downsampling operators

The downsampling operator with integer rate τ is given by

$$D_\tau([u]) = \frac{1}{\tau^2} \text{conv}_\tau(u, \mathbf{1}_\tau), \quad (\forall u), \quad (14)$$

where conv_τ denotes the bivariate convolution operation with striking sizes $\tau \times \tau$,⁵ and $\mathbf{1}_\tau$ is the all-ones matrix of size $\tau \times \tau$. The striking sizes define the size reduction in row and column directions. D_τ produces only the average intensity value of every $\tau \times \tau$ -block and hence it is not invertible without additional information of u .

3 Solution approaches

Solution approaches to the SIND problem should address three main tasks, including estimation of nonuniform defocus models, removal of nonuniform defocus effects, and reconstruction of an SR image. Assuming that the nonuniform defocus models have been estimated, this paper is devoted to the last two tasks. We first discuss regularization schemes for the SIND problem.

3.1 Regularization functions

SR methods often minimize a cost function consisting of data fidelity and regularization [3–5, 7, 8, 10, 14, 16–18, 22, 23, 28, 30, 31]. Data fidelity is typically a norm of the residual between the theoretical and the measured data while regularization is driven by the *a priori* known physical attributes of the solution. The latter pertains to each particular application and is the main difference between existing SR techniques. Total variation and Tikhonov regularization were considered in, *e.g.*, [3, 18]. The Bilateral Total Variation (BTV) was introduced in [3] and later adapted in [4, 14, 16, 28, 31]. In [14] BTV was used in combination with the Laplace operator while in [16] it was used in combination with another regularization to enhance the consistence of the gradient variation.

In this paper, the images are assumed to have intensities in $[0, 1]$, and the set of matrices satisfying this constraint is denoted by Ω . This constraint is easy to handle, but essential for the success of our proposed algorithms, where acceleration optimization mechanisms are exploited. Its effectiveness has been widely known in the literature of deconvolution, see, *e.g.*, [25, 29]. There are several approaches to this constraint, *e.g.*, the penalty approaches using the associated distance function or its square. In this paper, we make use of the *indicator function* [20]:

$$\iota_\Omega(x) = \begin{cases} 0 & \text{if } x \in \Omega, \\ \infty & \text{otherwise.} \end{cases} \quad (15)$$

⁵ The terminology is standard in the field of convolutional neural networks.

In our simulation results, this constraint is a precise regularization and hence its advantages over the other schemes are clearly observed, see Sect. 4.1.

3.2 The proposed algorithms

In view of Remark 2, the SIND problem can be addressed by solving (13) and (12) sequentially. For each $m = 1, 2, \dots, M$, (13) is the *single-frame nonuniform defocus removal* problem recently studied in [25]. Hence, it can be solved by the algorithm proposed in that paper, where its challenges including the typical ill-posedness were also discussed and global convergence of the proposed algorithm was also established. The main challenge of (12) is that the downsampling operator D_τ is not invertible, in particular, closed-form solutions for it are not available. We propose to apply the regularization (15) and make use of the fast proximal gradient method introduced in [2], often known as FISTA, for solving (12).

The algorithm resulted from this sequential approach will be referred to as the *Sequential Minimization* (SM) algorithm for the SIND problem. However, we chose to skip its details for the sake of brevity. The main advantages of the SM algorithm include its simplicity and the parallelism of (13) while its major disadvantage is the typical error amplification of multi-step optimization.

To overcome the drawback of SM, we next propose a new algorithm to simultaneously handle both Superresolution reconstruction And Nonuniform Defocus Removal (SANDR). The SANDR algorithm combines the nonuniform defocus removal method developed in [25] and the least squares approach [27] for subpixel image reconstruction but not in a sequential manner. Hence, it inherits global convergence from its two component techniques and avoids the typical error amplification of multi-step optimization contributing to its robustness, see Sects. 4.3&4.4. Making use of the acceleration techniques for optimization of FISTA assures fast convergence of the SANDR algorithm going from rate $\mathcal{O}(1/k)$ to $\mathcal{O}(1/k^2)$ compared to most existing SR techniques using the gradient descent method.

For simplicity, the noise covariance matrices \mathcal{W}_m in (11) are taken to be the identity matrix in the sequel. The repetitive term ($m = 1, 2, \dots, M$) following the subscript m will be omitted for brevity.

In the sequel, U_τ will denote a right inverse of the downsampling operator D_τ defined in (14), *i.e.*, $D_\tau \circ U_\tau = \text{Id}$, the identity mapping.⁶ U_τ can be understood as a numerical upsampling operator, and in our numerical results, it is taken to be the interpolation with block constant values. Recall that the translation by a vector with integer coordinates (v_x, v_y) , is given by

$$T_{(v_x, v_y)}(u)(r, c) = u(r - v_x, c - v_y), \quad (\forall u), \quad (16)$$

where (r, c) are the row-column coordinates of the pixels.

⁶ U_τ is not unique and in general $D_\tau \circ U_\tau \neq U_\tau \circ D_\tau$.

Algorithm 1 (the SANDR algorithm)

Input: i_m – LR images, B_m – blur operators, λ – stepsize, $t^{(0)}$ – initial acceleration stepsize, K – number of iterations, and $\varepsilon > 0$.

Initialization: $X^{(0)} = O^{(0)} = \frac{1}{M} \sum_{m=1}^M T_{(-\tau v_m)}(U_\tau(i_m))$.

Iteration process: given $X^{(k)}$, $O^{(k)}$, $t^{(k)}$

$$\begin{aligned} G_m^{(k)} &= T_{(-\tau v_m)} \circ U_\tau \left(\nabla f_m \left(D_\tau \circ T_{\tau v_m} \left(O^{(k)} \right) \right) \right), \\ X_m^{(k+1)} &= P_\Omega \left(O^{(k)} - \lambda G_m^{(k)} \right), \\ X^{(k+1)} &= \frac{1}{M} \sum_{m=1}^M X_m^{(k+1)}, \\ t^{(k+1)} &= \frac{1 + \sqrt{1 + 4t^{(k)^2}}}{2}, \\ O^{(k+1)} &= X^{(k+1)} + \frac{t^{(k)} - 1}{t^{(k+1)}} \left(X^{(k+1)} - X^{(k)} \right). \end{aligned}$$

Stopping criteria: $k > K$ or

$$\sum_{m=1}^M \left\| G_m^{(k)} \right\| > \sum_{m=1}^M \left\| G_m^{(k-1)} \right\| + \varepsilon. \quad (17)$$

Output: $\hat{O} = P_\Omega \left(O^{(\text{end})} \right)$.

In Algorithm 1, P_Ω is the projection operator associated with Ω and the functions f_m are given by

$$f_m(x) = \frac{1}{2} \|B_m(x) - i_m\|^2, \quad (m = 1, 2, \dots, M).$$

4 Numerical simulations

As explained in Sect. 2.2, a higher degree of defocus in an (LR) image corresponds to a larger number of defocus zones and smaller supports (nonzero entries) of the mask functions and vice versa. To simplify simulation of random defocus levels in LR images, we chose to fix these parameters, but consider the DoF d in (7) as the single parameter quantifying the defocus in each image, called the *blur coefficient* of the image in the sequel. It is important to mention that our choice for convenience does not contradict the fact that DoF is a fixed physical parameter of the camera because underestimation of DoF does not introduce model deviations.⁷ The larger the blur coefficient is, the more the defocus blur in the image.

Simulation data is generated according to the forward imaging model (9). Except for the analysis regarding the number of input images in Sect. 4.5,

⁷ It only costs computational time as the number of defocus zones increases accordingly.

Table 1 Parameters used in Sect. 4. M is the number of LR images, μ – size of the supports of mask functions in pixel rows/columns, ρ – PSF size (square), τ – SR factor, λ – stepsize, and $t^{(0)}$ – initial acceleration stepsize.

Parameter	M	μ	ρ	τ	λ	$t^{(0)}$
Value	4	3	11	2	1	1

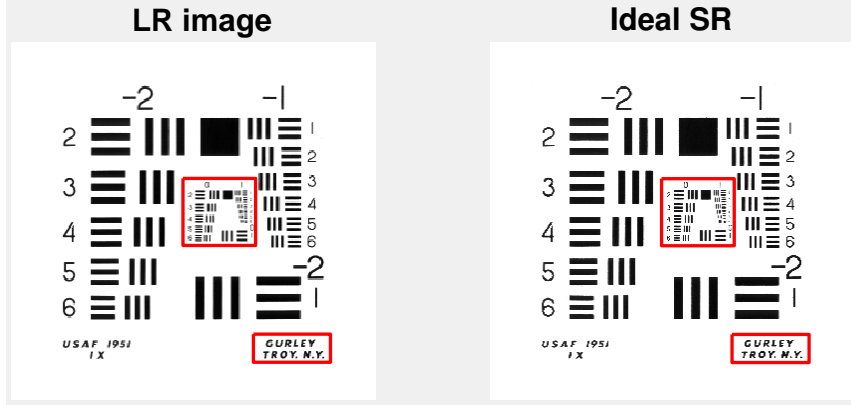


Fig. 2 LR image (left) and the ideal SR (right). The ROIs are shown in Fig. 3 for visual comparison of different SR methods.

each data set consists of four images corresponding to the shift vectors $v_1 = (0, 0)$, $v_2 = (1/2, 0)$, $v_3 = (0, 1/2)$ and $v_4 = (1/2, 1/2)$. Half of the images contain defocus blur varying in the vertical direction and half in the horizontal direction. Unless otherwise specified, the common parameters are as in Table 1.

Except for the noise analysis in Sect. 4.4, the data is corrupted with Poisson noise using the MATLAB function `imnoise`. The quality of SR reconstruction is measured by the *Root Mean Square* (RMS) error of the restored SR image relative to the ideal one: $\|\hat{O} - O\|/\|O\|$. The stopping criterion (17) is not implemented as it is not so relevant for simulations.

As no algorithms are available to address the SIND problem, we can only demonstrate its advantages over other SR methods neglecting the defocus effects. It is important to mention that the Projected Gradient (PG) and the Sequential Minimization (SM) algorithms are also first considered for the SIND problem, and hence comparing the SANDR algorithm with them is not a goal of this section. Instead, their own advantages and disadvantages in various problem settings will be of our primary interest.

4.1 Comparison to known SR methods

Most existing SR methods minimize a cost function consisting of data fidelity and regularization using the gradient descent method [4, 7, 8, 14, 16, 22, 28, 30, 31].

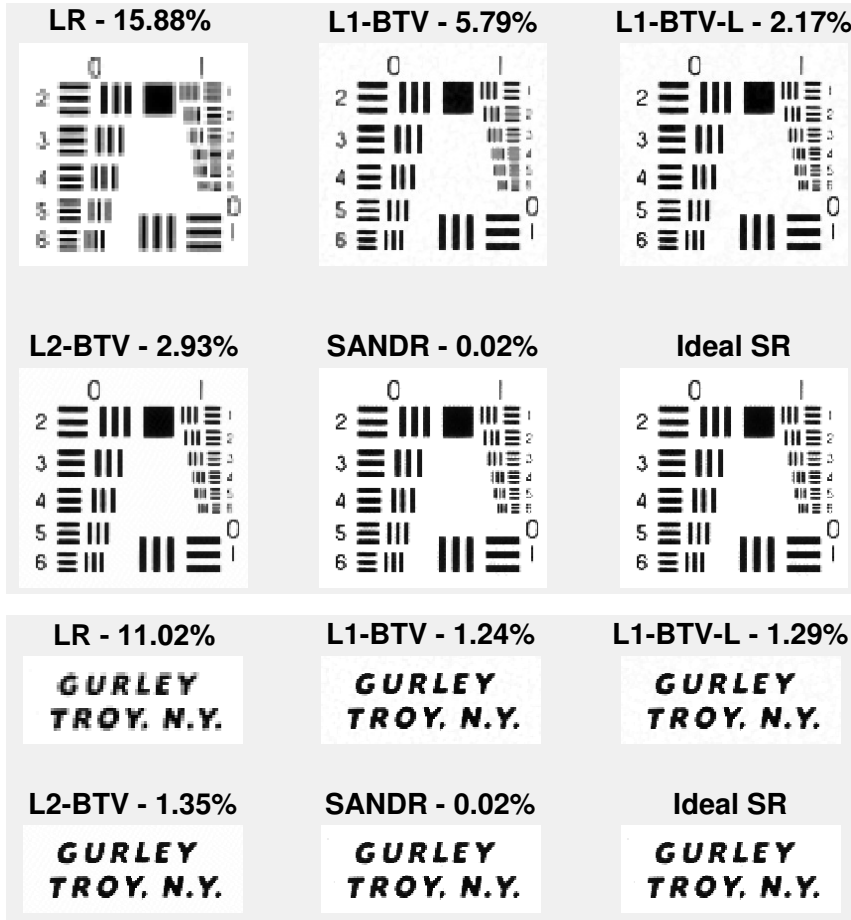


Fig. 3 SR images obtained by L1-BTV, L1-BTV-L, L2-BTV and SANDR are shown together with an LR image and the ideal SR. Only the ROIs are shown for clarity. The relative RMS error of each ROI is also reported. The SANDR algorithm outperforms the other SR methods.

Data fidelity is typically the (weighted) L_p -norm ($1 \leq p \leq 2$) of the residual between the theoretical and the measured data while regularization is driven by the *a priori* known physical attributes of the solution, see Sect. 3.1. In this section, we compare the SANDR algorithm with three existing SR methods minimizing (1) the L_1 -norm with bilateral total variation (L1-BTV) [4], (2) the L_1 -norm with BTV and Laplace operator (L1-BTV-L) [14], and (3) the L_2 -norm with BTV (L2-BTV) [28]. Each iteration of the algorithms is additionally followed by a projection on the constraint Ω to improve their performance, especially in terms of stability. Note that without defocus effects, the SM and the SANDR algorithms coincide.

Figure 2 shows an LR image (left) and the ideal SR (right). The SR images obtained by L1-BTV, L1-BTV-L, L2-BTV and SANDR are shown in Fig. 3

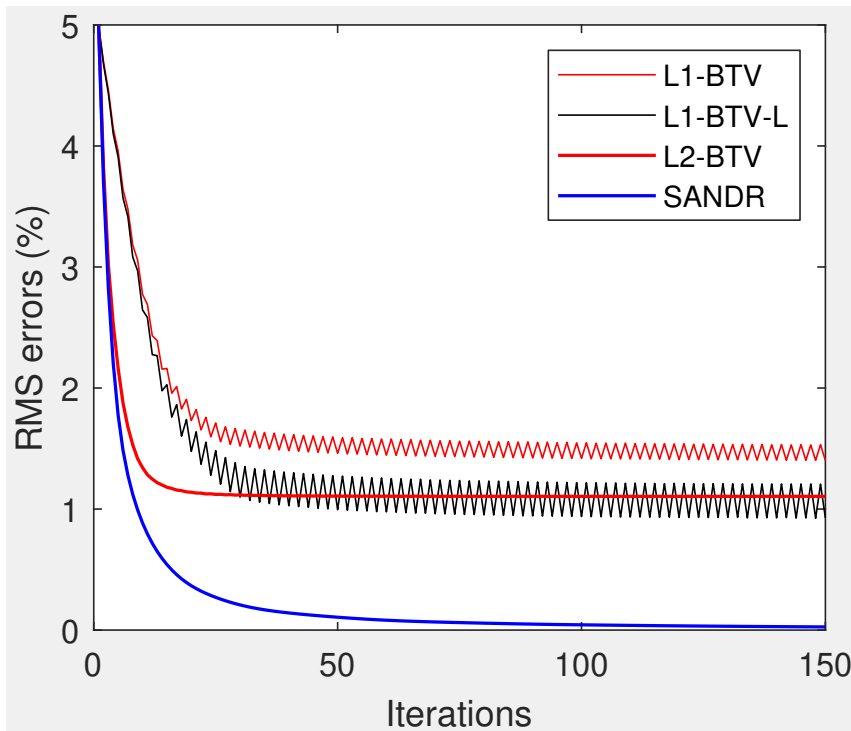


Fig. 4 Relative RMS errors of the SR images obtained by L1-BTV, L1-BTV-L, L2-BTV and SANDR are shown in iterations. The SANDR algorithm is superior to the other methods in both convergence speed and accuracy.

together with an LR image and the ideal SR. Only the ROIs are shown for clarity. The relative RMS error of each ROI is also reported. The SANDR algorithm clearly outperforms the other methods both visually and in terms of RMS errors. This is further explained in Fig. 4, where the RMS errors are shown in iterations. The SANDR algorithm is far superior to the others in both convergence speed and accuracy. Faster convergence is due to the acceleration feature of SANDR while higher accuracy can be explained by the fact that Ω is a precise regularization in this simulation problem. Ripple behaviours of L1-BTV and L1-BTV-L in Fig. 4 can be explained by the step-size being larger than the distance from the iteration to a local minimum. This phenomenon is more likely to happen to L_1 -norm cost functions since their gradient includes the sign function, which does not depend on the residual gap of the current iteration.⁸ Gradually decreasing the stepsize is a possible remedy for this issue, however, we chose not to distract the reader further in that direction because there does not exist a unified recipe for such tasks while the methods are not applicable to the SIND problem.

⁸ An advantage of L_1 -norm cost functions is their potential to suppress outliers.

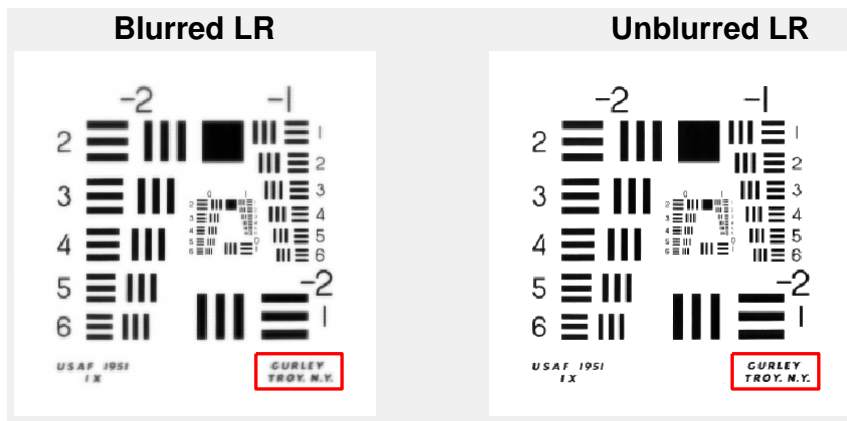


Fig. 5 LR image with defocus varying in the vertical direction (left) and the unblurred one (right).

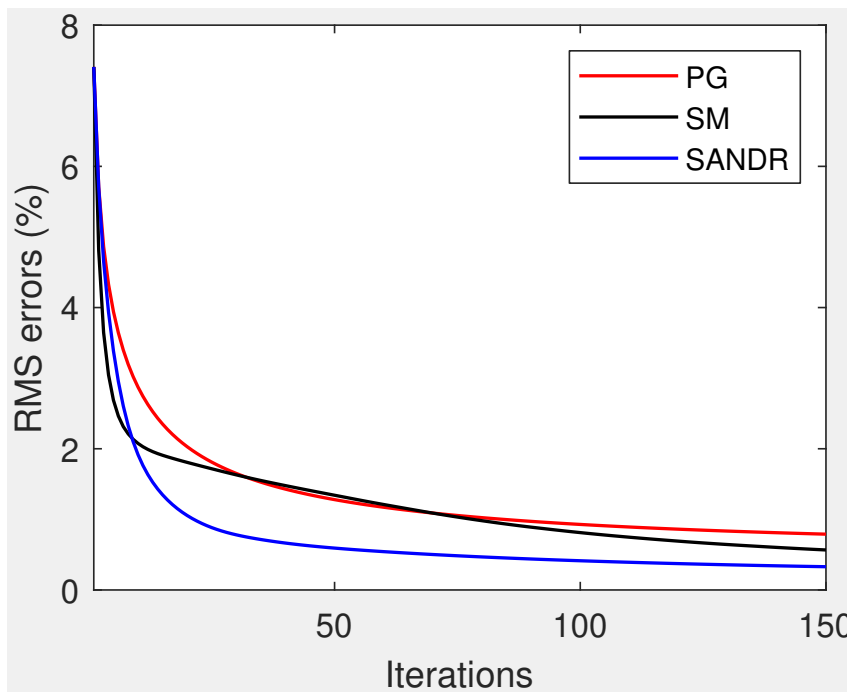


Fig. 6 RMS errors of the SR images obtained by PG, SM and SANDR are shown in iterations. The algorithms exhibit convergence properties and without acceleration, PG (red) converges slower than SM (black) and SANDR (blue). The RMS error with 150 PG iterations is 0.79%, corresponding to about 30 iterations of SANDR.

Table 2 Parameters used in Sect. 4.3. d_{\max} is the upper bound of (random) blur coefficients, N – # defocus zones, n_0 – focal position, (l, w) – size of LR images, and K – # iterations.

Parameter	d_{\max}	N	n_0	$l = w$	K
Value	0.06 – 0.3	55	28	165	50

4.2 Convergence properties

In this section, we demonstrate convergence properties of the SANDR algorithm along with the PG and SM methods. We consider LR images of size 330×330 pixels with 110 defocus zones and blur coefficients randomly taken in the interval $[0.001, 0.06]$. The other parameters are as in Table 1. One of the LR images with defocus effects varying in the vertical direction and its unblurred version are shown in Fig. 5.

In Fig. 6 the RMS errors of the SR images obtained by PG, SM and SANDR are shown in iterations. The algorithms exhibit convergence properties and without acceleration, PG (red) converges slower than SM (black) and SANDR (blue). The RMS error with 150 iterations of PG is 0.79%, corresponding to about 30 iterations of SANDR. In Fig. 7 the ROIs of the SR images obtained by 5, 15, 50 and 150 iterations of PG, SM and SANDR are shown in comparison with the ones of an LR image and the ideal SR. The relative RMS error of each ROI is also shown. Note that the RMS error of each unblurred LR image is around 13.83%.

4.3 Solvability analysis

As explained at the beginning of Sect. 4, *blur coefficients* quantify the defocus in the LR images. The larger they are, the more challenging the SIND problem is. In this section, we analyse the solvability of PG, SM and SANDR with respect to this parameter. For each experiment, four blur coefficients of the LR images are randomly taken in the interval $[0.001, d_{\max}]$ with d_{\max} ranging from 0.06 to 0.3. The other parameters are as in Table 2.⁹

For each value of d_{\max} , one hundred experiments with PG, SM and SANDR are reported in Fig. 8, where the RMS errors of the obtained SR images with respect to the ideal one are presented. The restoration errors increase for larger values of d_{\max} . SM works best for d_{\max} up to 0.06, but it quickly becomes problematic for d_{\max} from 0.12 due to its sequential optimization. SANDR is effective for blur coefficients up to 0.3. It outperforms PG and SM (for $d_{\max} \geq 0.12$) in both accuracy and consistency, and the superiority becomes more significant for larger d_{\max} . Higher accuracy is reflected by its smaller average restoration errors while more consistency is indicated by its smaller variances of the errors. To visualize the *blur coefficient* parameter, the PSFs

⁹ It is a trade-off between the computational complexity (number of iterations) and the restoration accuracy, in view of Figs. 4 and 6 we chose to run 50 iterations for each experiment.

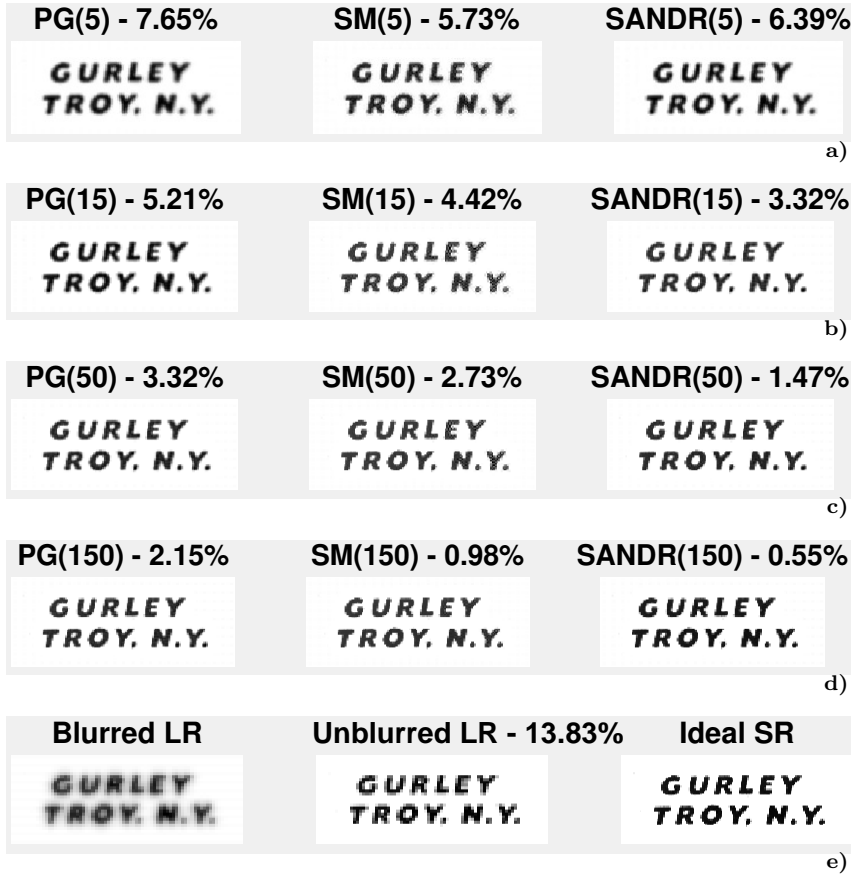


Fig. 7 ROIs of the SR images obtained by a) 5, b) 15, c) 50, d) 150 iterations of PG, SM and SANDR are shown in comparison with e) the ones of an LR image and the ideal SR. The RMS error of each ROI is also shown. The RMS error of each unblurred LR image is around 13.83%.

for the 30th and 50th defocus zones (counted from the focal position) with blur coefficient 0.06 are shown in Fig. 9. Recall that the distortion level of an image is proportional to the product of the blur coefficient and the zone position in view of (7).

4.4 Noise analysis

We analyse the influence of noise on the performance of PG, SM and SANDR. Five levels of Gaussian noise ranging from 45 to 65 dB (decibels) are considered. Recall that the signal-to-noise ratio (SNR) in decibels is defined by: $\text{SNR} = 10 \ln(P/P_0)$, where P and P_0 are the powers of the signal and noise,

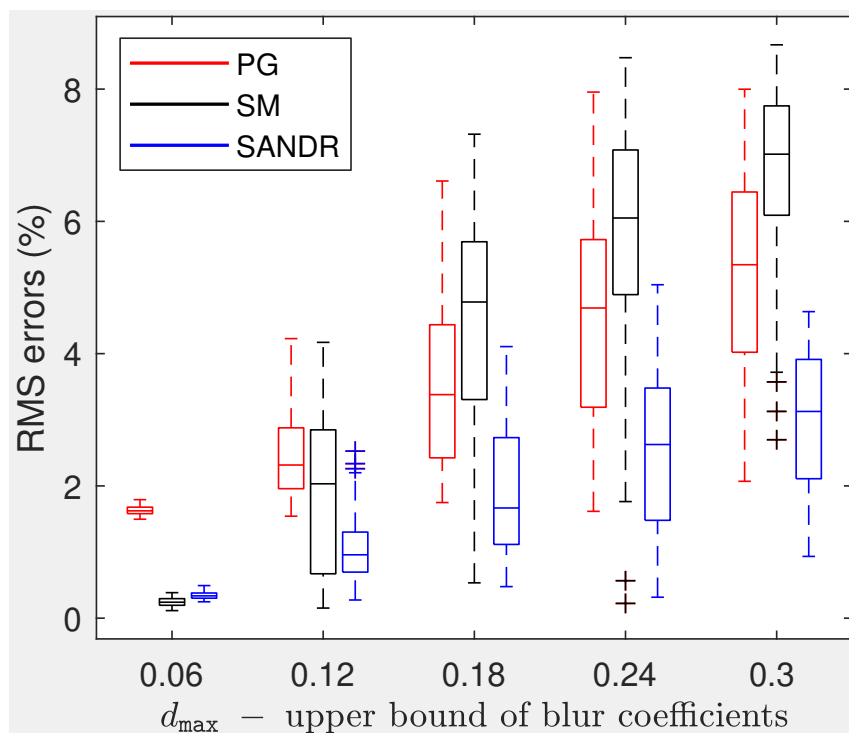


Fig. 8 Solvability analysis of PG, SM and SANDR with respect to the distortion level of data images quantified by the *blur coefficients*. One hundred experiments are reported for each value of d_{\max} ranging from 0.06 to 0.3. The restoration errors increase for larger d_{\max} . SM works best for d_{\max} up to 0.06, but it quickly becomes problematic for d_{\max} from 0.12 due to its sequential optimization. SANDR is effective for blur coefficients up to 0.3 and outperforms PG and SM (for $d_{\max} \geq 0.12$) in both accuracy and consistency. The superiority becomes more significant for larger values of d_{\max} .

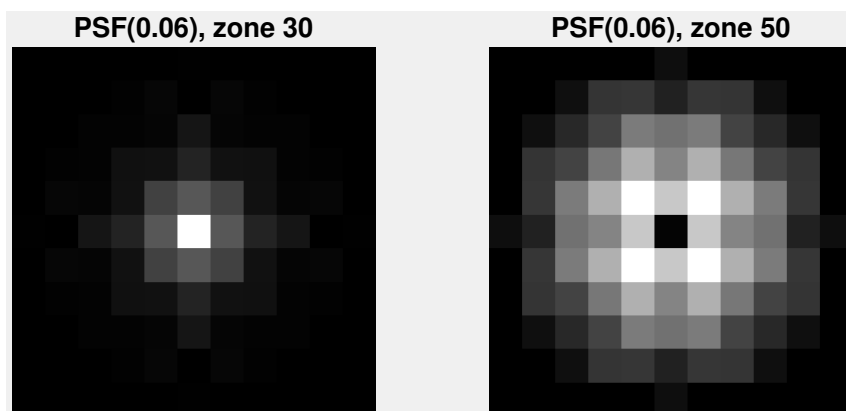


Fig. 9 PSFs for the 30th (left) and 50th (right) defocus zones with blur coefficient 0.06.

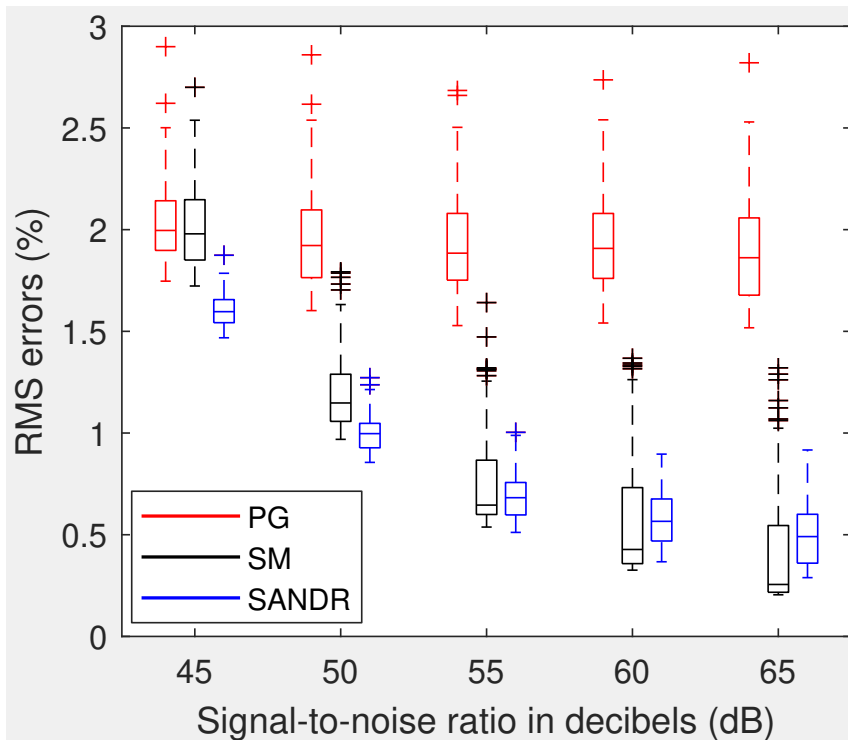


Fig. 10 Noise analysis of PG, SM and SANDR. One hundred experiments are reported for each SNR from 45 to 65 dB. The reconstruction is more accurate for higher SNR. SM works best for SNR from 55 dB, but it quickly becomes problematic for SNR decreasing from 50 dB. Since SM and SANDR are acceleration variants of PG, they are less robust than PG.

respectively. To visualize the noise, an LR image with SNR 45 dB is shown in Fig. 12 together with its residual relative to the noiseless one.

For each SNR, one hundred experiments with $d_{\max} = 0.09$ and the other parameters as in Table 2 are reported in Fig. 10, where the RMS errors of the SR images obtained by PG, SM and SANDR are presented. The reconstruction is more accurate for higher SNR. SM works best for SNR from 55 dB, but it quickly becomes problematic for SNR decreasing from 50 dB. Its less robustness against noise compared to SANDR is due to its two-step optimization, see also Sect. 4.3. It is not a surprise that SM and SANDR are less robust than PG because the former are acceleration variants of the latter and there is a typical trade-off between robustness and convergence speed. In view of Fig. 10, it is worth thinking about PG for the SIND problem with SNR below 45 dB, but for higher SNR it is outperformed by the others. It is important to recall that the conclusions drawn for the SM algorithm from Fig. 10 are valid only for d_{\max} up to 0.09, which seems to be a limit for it, see also Fig. 8. To demonstrate this point, we do similar experiments but with slightly larger blur coefficients, $d_{\max} = 0.12$ in place of 0.09. The results are summarized in Fig.

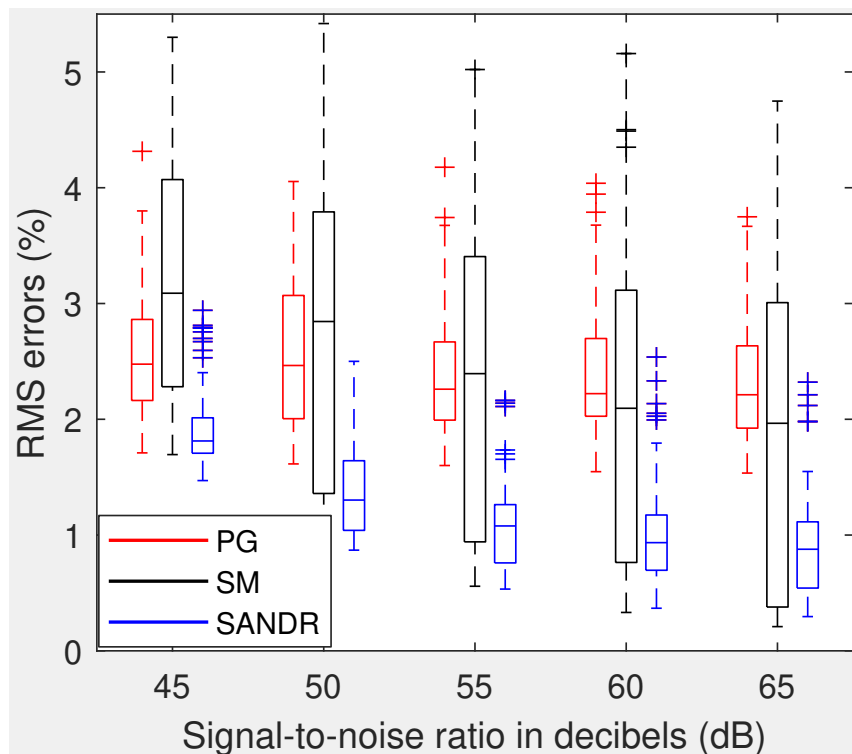


Fig. 11 Experiments similar to those reported in Fig. 10 but with $d_{\max} = 0.12$ instead of 0.09 show that SM deteriorates much faster than PG and SANDR for larger blur coefficients.

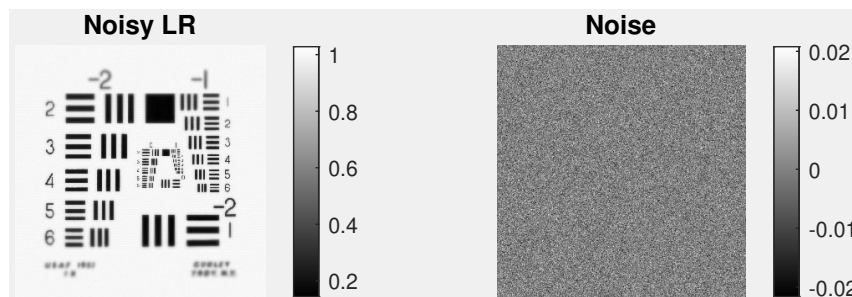


Fig. 12 A noisy LR image (left) with SNR 45 dB and its residual (right) with respect to the noiseless one.

11, where SM deteriorates much more than PG and SANDR in comparison with Fig. 10.

Table 3 Parameters used in Sect. 4.6. d_{\max} is the upper bound of blur coefficients, N – # defocus zones, n_0 – focal position, (l, w) – size of LR images, and K – # iterations.

Parameter	d_{\max}	N	n_0	$l = w$	K
Value	0.09	85	43	255	50

4.5 Number of input images

The major practical challenge of SR by subpixel motions is to perform the shifts accurately. Let us suppose that we are able to perform shifts at scale $1/\tau$ pixel, where $1 < \tau \in \mathbb{Z}$.¹⁰ Then there are at most τ^2 LR images and one cannot expect to gain a SR factor greater than τ . In this section, we briefly study the influence of the number of input images on the quality of SR. We consider $\tau = 4$ and construct the SR image using 2, 4, 8 and 16 LR images, respectively. In this experiment, $d_{\max} = 0.06$ and the other parameters are as in Table 2.

The numerical results are summarized in Fig. 13, where only the ROIs and their RMS errors are shown for brevity. It is clear that more input images result in higher quality of the SR and the observation is consistent for PG, SM and SANDR. SR images obtained with two LR images (the first row) already shows improvement even in comparison with the unblurred LR images (the second in the last row).

4.6 Image cropping

Cropping the data images would introduce deviations to the imaging model (9). This issue does not arise in the previous sections since the simulation object there has almost constant intensity near the boundary. In this section, we study the influence of image cropping on the performance of the PG, SM and SANDR algorithms.

Four images are generated according to (9) with the parameters as in Table 3. They are then windowed using Butterworth function to yield the LR images, one of which is shown at the bottom left of Fig. 14. The SR images obtained by PG, SM and SANDR are shown in Fig. 14 in comparison with an LR image and the ideal SR. The SANDR algorithm is the most effective for this problem while the SM algorithm is problematic due to high level of defocus effect as discussed in Sect. 4.3. The SM and SANDR algorithms suffer more boundary effects than PG since the former are more sensitive to noise than the latter as analyzed in Sect. 4.4. To reduce the restoration errors near the boundary, the Butterworth filter also need to be applied to every iteration update of the algorithms. The RMS errors are computed for the central regions with 90% in radius of the images. The reconstruction error is smaller in the central region and increases towards the boundary. The ROIs are zoomed out in Fig. 15 for a better inspection of finer details. The RMS error of each ROI is also reported.

¹⁰ In this study, inaccuracy of subpixel registration is subsumed in noise.

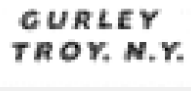
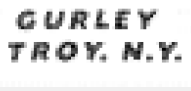
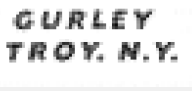
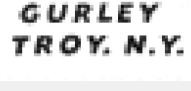
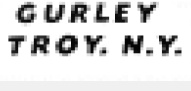
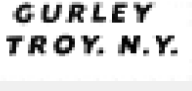
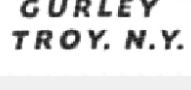
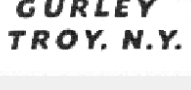
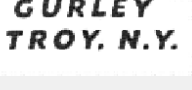
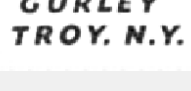





PG(2) - 7.05% 	SM(2) - 7.04% 	SANDR(2) - 7.03% 
PG(4) - 6.93% 	SM(4) - 6.92% 	SANDR(4) - 6.91% 
PG(8) - 2.08% 	SM(8) - 1.28% 	SANDR(8) - 1.27% 
PG(16) - 1.91% 	SM(16) - 0.59% 	SANDR(16) - 0.61% 
Blurred LR 	Unblurred LR - 17.18% 	Ideal SR 

Fig. 13 Influence of the number of input images on the SR images obtained by PG, SM and SANDR. ROIs of the SR images obtained with 2, 4, 8 and 16 LR images are shown together with their RMS errors. More input images result in higher quality of SR.

5 Concluding Remarks

We have investigated the problem of constructing an object with high-resolution using several nonuniform defocused images, called the SIND problem. Nonuniform defocus effects can arise in both standard techniques of data registration, including the use of multiple cameras and moving the object. However, the SIND problem has not been studied before. We have proposed the efficient algorithm for SIND, called the SANDR algorithm, that can process both subpixel image reconstruction and nonuniform defocus removal simultaneously. Important theoretical and practical aspects of the SANDR algorithm have been analyzed, including its global convergence, solvability, noise robustness, dependence on the number of LR images, and sensitivity to model deviations due to image cropping. We have demonstrated advantages of the SANDR algorithm over a number of existing superresolution methods without considering defocus effects because the latter cannot handle this additional challenge. Our

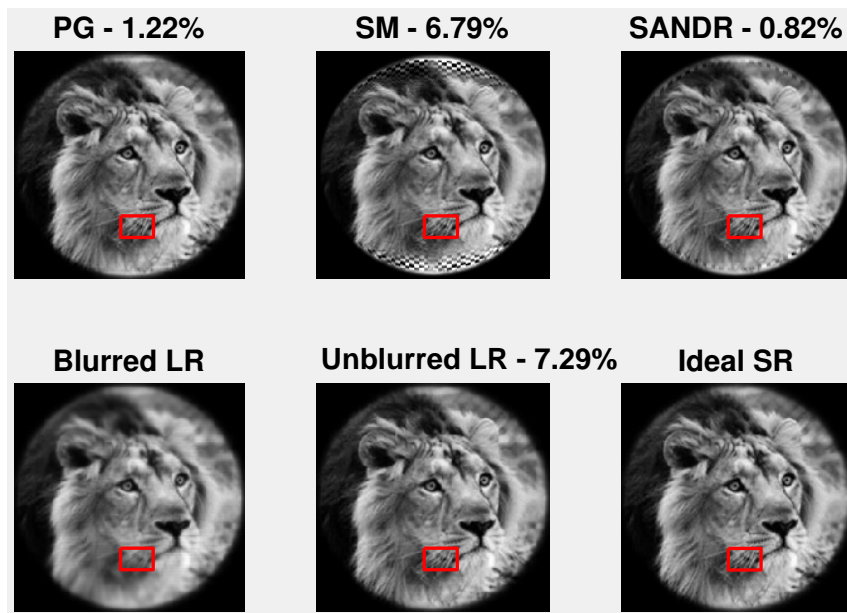


Fig. 14 SR images obtained by PG, SM and SANDR are shown together with an LR image (bottom left) and the ideal SR (bottom right). The restoration error is smaller in the central region and becomes larger towards the boundary. The SANDR algorithm is the most effective for this problem while the SM algorithm is problematic due to high level of defocus effect. The SANDR and SM algorithms suffer more boundary effects than PG.

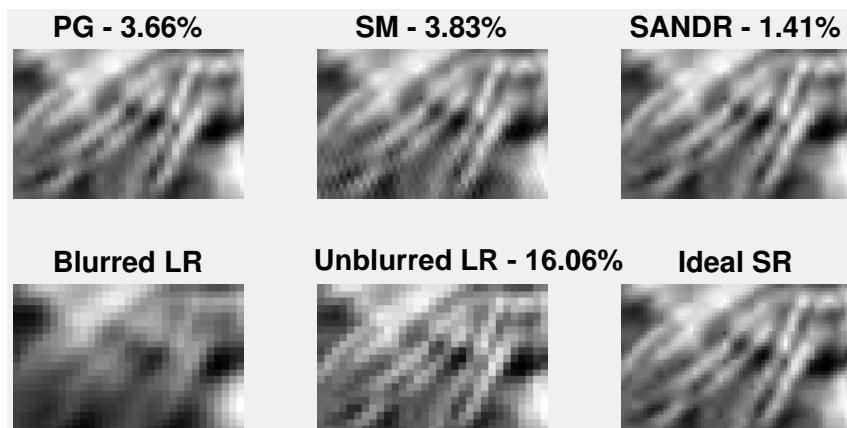


Fig. 15 The ROIs marked in Fig. 14 are shown for a better inspection of finer details. Their RMS errors with respect to the ideal SR are also reported.

consideration was primarily motivated by the inspection of wafers in semiconductor industry, but the SANDR algorithm can be scalable for similar applications of computer vision in Industry 4.0.

Funding. This project has received funding from the ECSEL Joint Undertaking (JU) under grant agreement No. 826589. The JU receives support from the European Union’s Horizon 2020 research and innovation programme and Netherlands, Belgium, Germany, France, Italy, Austria, Hungary, Romania, Sweden and Israel.

References

1. B. Bascle, A. Blake, and A. Zisserman. Motion deblurring and super-resolution from an image sequence. In Bernard Buxton and Roberto Cipolla, editors, *Computer Vision — ECCV ’96*, pages 571–582, Berlin, Heidelberg, 1996. Springer Berlin Heidelberg.
2. A. Beck and M. Teboulle. A fast iterative shrinkage-thresholding algorithm for linear inverse problems. *SIAM J. Imaging Sci.*, 2(1):183–202, 2009.
3. S. Farsiu, D. Robinson, M. Elad, and P. Milanfar. Fast and robust super-resolution. In *Proceedings 2003 International Conference on Image Processing (Cat. No.03CH37429)*, volume 2, pages II–291, 2003.
4. S. Farsiu, M. D. Robinson, M. Elad, and P. Milanfar. Fast and robust multiframe super resolution. *IEEE Transactions on Image Processing*, 13(10):1327–1344, 2004.
5. Sina Farsiu, Dirk Robinson, Michael Elad, and Peyman Milanfar. Robust shift and add approach to superresolution. In Andrew G. Tescher, editor, *Applications of Digital Image Processing XXVI*, volume 5203, pages 121 – 130. International Society for Optics and Photonics, SPIE, 2003.
6. J. W. Goodman. *Introduction to Fourier Optics*. Roberts & Company Publishers, 2005.
7. Hidenori Takeshima and Toshimitsu Kaneko. Image registration using subpixel-shifted images for super-resolution. In *2008 15th IEEE International Conference on Image Processing*, pages 2404–2407, 2008.
8. S. Huang, J. Sun, Y. Yang, Y. Fang, and P. Lin. Multi-frame super-resolution reconstruction based on gradient vector flow hybrid field. *IEEE Access*, 5:21669–21683, 2017.
9. Szu-Hao Huang and Ying-Cheng Pan. Automated visual inspection in the semiconductor industry: A survey. *Computers in Industry*, 66:1–10, 2015.
10. Michal Irani and Shmuel Peleg. Improving resolution by image registration. *CVGIP: Graphical Models and Image Processing*, 53(3):231–239, 1991.
11. A. V. Kanaev and C. W. Miller. Multi-frame super-resolution algorithm for complex motion patterns. *Opt. Express*, 21(17):19850–19866, 2013.
12. S.P. Kim, N.K. Bose, and H.M. Valenzuela. Recursive reconstruction of high resolution image from noisy undersampled multiframe. *IEEE Transactions on Acoustics, Speech, and Signal Processing*, 38(6):1013–1027, 1990.
13. S.P. Kim and W.-Y. Su. Recursive high-resolution reconstruction of blurred multiframe images. *IEEE Trans Image Process.*, 2(4):534–542, 1993.
14. Amine Laghrib, Abdelghani Ghazdali, Abdelilah Hakim, and Said Raghay. A multi-frame super-resolution using diffusion registration and a nonlocal variational image restoration. *Computers and Mathematics with Applications*, 72(9):2535–2548, 2016.
15. Eun Sil Lee and Moon Gi Kang. Regularized adaptive high-resolution image reconstruction considering inaccurate subpixel registration. *IEEE Transactions on Image Processing*, 12(7):826–837, 2003.
16. Xuelong Li, Yanting Hu, Xinbo Gao, Dacheng Tao, and Beijia Ning. A multi-frame image super-resolution method. *Signal Processing*, 90(2):405–414, 2010.
17. Mikhail Loktev, Oleg Soloviev, Svyatoslav Savenko, and Gleb Vdovin. Speckle imaging through turbulent atmosphere based on adaptable pupil segmentation. *Opt. Lett.*, 36(14):2656–2658, 2011.
18. Nhat Nguyen, P. Milanfar, and G. Golub. A computationally efficient superresolution image reconstruction algorithm. *IEEE Transactions on Image Processing*, 10(4):573–583, 2001.

19. Shmuel Peleg, Danny Keren, and Limor Schweitzer. Improving image resolution using subpixel motion. *Pattern Recognition Letters*, 5(3):223–226, 1987.
20. R. T. Rockafellar and R. J. Wets. *Variational Analysis*. Grundlehren Math. Wiss. Springer-Verlag, Berlin, 1998.
21. K. Sauer and J. Allebach. Iterative reconstruction of bandlimited images from nonuniformly spaced samples. *IEEE Transactions on Circuits and Systems*, 34(12):1497–1506, 1987.
22. F. Sroubek, G. Cristobal, and J. Flusser. A unified approach to superresolution and multichannel blind deconvolution. *IEEE Transactions on Image Processing*, 16(9):2322–2332, 2007.
23. Sung Cheol Park, Min Kyu Park, and Moon Gi Kang. Super-resolution image reconstruction: a technical overview. *IEEE Signal Processing Magazine*, 20(3):21–36, 2003.
24. Hiroyuki Takeda, Peyman Milanfar, Matan Protter, and Michael Elad. Super-resolution without explicit subpixel motion estimation. *IEEE Transactions on Image Processing*, 18(9):1958–1975, 2009.
25. Nguyen Hieu Thao, Oleg Soloviev, Jacques Noom, and Michel Verhaegen. Nonuniform defocus removal for image classification. Manuscript submitted to IEEE Transactions on Image Processing in February 2021.
26. Hanoch Ur and Daniel Gross. Improved resolution from subpixel shifted pictures. *CVGIP: Graphical Models and Image Processing*, 54(2):181–186, 1992.
27. Michel Verhaegen and Vincent Verdult. *Filtering and System Identification: A Least Squares Approach*. Cambridge University Press, 2007.
28. Longguang Wang, Zaiping Lin, Xinpu Deng, and W. An. Multi-frame image super-resolution with fast upscaling technique. *arXiv: Computer Vision and Pattern Recognition*, 2017.
29. Dean Wilding, Oleg Soloviev, Paolo Pozzi, Gleb Vdovin, and Michel Verhaegen. Blind multi-frame deconvolution by tangential iterative projections (TIP). *Opt. Express*, 25(26):32305–32322, 2017.
30. Liangpei Zhang, Qiangqiang Yuan, Huanfeng Shen, and Pingxiang Li. Multiframe image super-resolution adapted with local spatial information. *J. Opt. Soc. Am. A*, 28(3):381–390, 2011.
31. N. Zhao, C. Li, H. Shi, and C. Lin. Multi-frame image super-resolution based on regularization scheme. In *2011 International Conference on Control, Automation and Systems Engineering (CASE)*, pages 1–4, 2011.
32. Qinbang Zhou, Renwen Chen, Bin Huang, Chuan Liu, Jie Yu, and Xiaoqing Yu. An automatic surface defect inspection system for automobiles using machine vision methods. *Sensors*, 19(3), 2019.